Catalysis Letters (2021) 151:1231–1238
https://doi.org/10.1007/s10562-020-03398-3

Efficient Improved Charge Separation of FeP Decorated Worm-Like Nanoporous $BiVO_4$ Photoanodes for Solar-Driven Water Splitting

Jianhua Ge[1,2] · Xiulong Ding[1] · Daochuan Jiang[2] · Lei Zhang[2] · Pingwu Du[2]

Received: 4 July 2020 / Accepted: 17 September 2020 / Published online: 27 September 2020

Abstract

Photoelectrochemical (PEC) water splitting using $BiVO_4$ semiconductor photoanodes have been appealed to plenty of attentions in the past few decades. In this study, FeP was used as an active precious-metal-free cocatalyst for the first time to enhance the performance of worm-like nanoporous $BiVO_4$ photoanodes for PEC water splitting. Characterization results demonstrate that FeP nanoparticles were successfully deposited on surface of the pritine $BiVO_4$ photoanodes, and served as an noble metal-free cocatalyst for solar-driven PEC water splitting. Furthermore, a maximum photocurrent density of ~ 3.05 mA/cm^2 at 1.23 V vs RHE could be achieved by loading moderate amount of FeP on the surface of $BiVO_4$, which is about 1.6 times higher than that of the unmodified $BiVO_4$. Meanwhile, the efficient suppression of surface recombination by FeP was also confirmed by the PEC measurements in Na_2SO_3 solution. The maximum ABPE of FeP/$BiVO_4$ photoanodes was ~ 0.53% at 0.60 V vs RHE, indicating the potential application for overall solar-driven water splitting.

Graphic Abstract

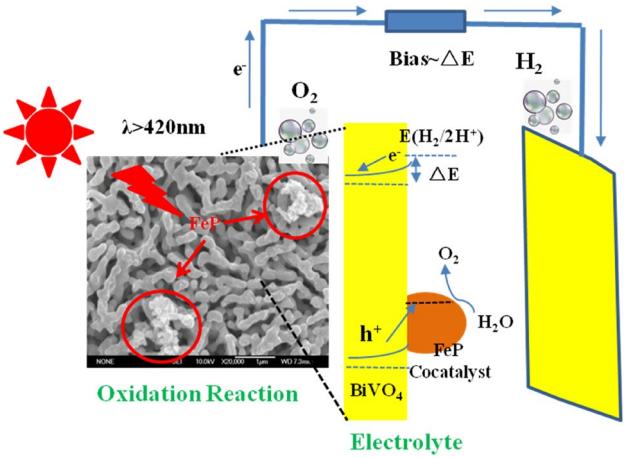

Keywords $BiVO_4$ · Photoanodes · FeP · Water splitting · Charge separation

1 Introduction

Since the groundbreaking work of Fujishima and Honda was published in 1972, photoelectrochemical (PEC) water splitting using semiconductor photoanodes materials to produce hydrogen and oxygen, is widely regarded as a promising route to settle the energy crisis worldwide in the future [1–6]. To date, a considerable number of photoanode

✉ Jianhua Ge
gejianhua13@163.com

✉ Pingwu Du
dupingwu@ustc.edu.cn

Extended author information available on the last page of the article

materials, such as TiO_2 [7–10], WO_3 [11–14], α-Fe_2O_3 [15–18], Ta_3N_4 [19–23], and $BiVO_4$ [24–26] and so on, have been extensively developed by scientists. Among these candidates, $BiVO_4$, as an n-type semiconductor, is identified as a promising photoanode material for PEC water splitting, on account of its appropriate valance band level, visible-light response, excellent physicochemical stability, nontoxic, and low-cost. Unfortunately, bare $BiVO_4$ photoanodes always suffer from sluggish charge mobility, and fast surface charge recombination at the interface of the photoanode [27]. Therefore, tremendous effective strategies have been adopted, including surface modification [25], together with other semiconductors [28], and element doping [29], to alleviate the bottleneck of bare $BiVO_4$ photoanode. Specially, surface modification using cocatalysts, made up of earth-abundant elements, were considered as a convenient, low-cost and reproducible pathway to handled above-mentioned problems [24, 30–33]. For example, our group recently demonstrated that CoP nanoparticles can act as a noble metal-free cocatalyst on α-Fe_2O_3 photoanode to improve photoelectrochemical solar-driven water splitting for the first time [15]. Ding and coworkers reported the use of Co–borate as an efficient cocatalyst by electrodeposited onto the surface of $BiVO_4$ photoanode, which exhibits high PEC stability and performance [31]. Yu and cooperators found that the use of ferrihydrite as hole-storage layer to reduce the interface recombination for $BiVO_4$ PEC, resulting in a remarkable photocurrent density of 4.78 mA/cm^2 at as low as 0.6 V vs RHE [34]. Jason and collaborators fabricated FeOOH/$BiVO_4$ photoanode by a simple electro-deposition and heat treatment process, which exhibitied significantly improved photocurrent and stability for photoelectrochemical water splitting [35].

More recently, Fe_xP (x = 1 or 2), which is made of earth-abundant elements, can be used as a good electrocatalyst for H_2 production due to its enhancing the electronic conductivity [36–38]. Meanwhile, it was also found that Fe_2P were utilized as an active cocatalyst to enhance photocatalytic hydrogen production [39, 40]. However, to the best of our knowledges, the use of FeP as a cocatalyst on $BiVO_4$ photoanodes using the drop casting method for PEC water splittingr has rarely been received prior investigation.

Motivated by above mentioned analysis, in this study, pure $BiVO_4$ photoanodes with nanoporous morphology were initially synthesized to effectively increase the bulk charge separation. Furthermore, for the first time, we employ low-cost FeP nanoparticles as an effective cocatalyst to modify the surface of nanoporous $BiVO_4$ photoanodes, leading to the highly efficient suppression of surface recombination for PEC water splitting. The resulting FeP/$BiVO_4$ photoanode achieved a improved photocurrent density of ~ 3.05 mA/cm^2 at 1.23 V vs RHE under AM 1.5G illumination. Meanwhile, the surface charge recombination could be effectively suppressed by decorating photoanode with earth-abundant cocatalyst FeP nanoparticles.

2 Experimental Section

2.1 Materials

Chemicals (analytical grade) in this experiments, mainly including bismuth nitrate pentahydrate [$Bi(NO_3)_3{\cdot}5H_2O$, 99.0% purity], potassium iodide (KI, 99.0% purity), p-benzoquinone ($C_6H_4O_2$, 99.0% purity), vanadium(IV) oxy acetylacetonate [$VO(acac)_2$, 98.0% purity], Iron(III) chloride($FeCl_3$, 99.0% purity), sodium hypophosphite monohydrate ($NaH_2PO_2{\cdot}H_2O$, 98.0% purity), and dimethyl sulfoxide (DMSO, 99.0% purity), were all purchased from Aldrich or Aladdin Reagent Co., Ltd. (China) and used without specially purification.

2.2 Preparation of FeP/$BiVO_4$ Photoanodes

$BiVO_4$ photoanodes samples were prepared according to the original literature developed by Kim and Chio [27]. Typically, ~ 3.32 g KI was added to ~ 50 mL of distilled water. The solution with the pH was adjusted to ~ 1.70 by s dilute HNO_3, then ~ 970.14 mg $Bi(NO_3)_3{\cdot}5H_2O$ was dissolved in the KI solution, which was mixed with ~ 20 mL of absolute ethanol solution containing ~ 497.26 mg *p*-benzoquinone. The BiOI film (1 cm × 1 cm) was obtained by electrodeposition at −0.1 V vs Ag/AgCl. The resulting film was rinsed with absolute ethanol carefully and dried at room temperature. ~ 75 μL of DMSO solution containing ~ 0.20 M $VO(acac)_2$ was dropped uniformly on the BiOI film (1 cm × 1 cm), which was annealed at 450 °C for ~ 2 h in air. Then, the as-annealed $BiVO_4$ electrodes were immerged in 1 M NaOH solution for ~ 20 min to remove the excessive V_2O_5, rinsed with deionized water and dried in air at room temperature.

FeP nanoparticles were synthesized by phosphorlysis of Fe_3O_4 prepared nanoparticles using a hydrothermal method [41]. In a typical synthesis procedure, ~ 1.35 g $FeCl_3$ $0.6H_2O$, ~ 0.72 g urea and ~ 25 mL of ethylene glycol (EG) were vigorously magnetic stirred at room temperature. Then, the mixtures were transferred into a ~ 50 mL autoclave for hydrothermal reaction at 200 °C for 3 h in a static state. The resulting black product was collected by centrifugation, washed with deionized water and absolute alcohol for three times, dried at 60 °C in vacuum overnight. Subsequently, ~ 0.10 g of the as-prepared Fe_3O_4 and ~ 0.50 g of $NaH_2PO_2{\cdot}H_2O$ were mixed together and grounded. Then, the mixtures were calcined at 300 °C for 2 h under N_2 atmosphere. The obtained black product was sufficiently washed with deionized water and dried at 80 °C ~ 24 h.

For comparison, Fe_2P nanoparticles were prepared by phosphorlysis of $FeCl_3$. In a typical synthesis procedure, ~ 1.0 g $FeCl_3$ $0.6H_2O$ and ~ 3.0 g of $NaH_2PO_2{\cdot}H_2O$ were mixed together and grounded. Then, the mixture was calcined at 300 °C for 2 h under N_2 atmosphere, washed with deionized water and dried at 60 °C overnight.

~ 1 mg of FeP nanoparticles were ultrasonic dispersed in ~ 1 mL of absolute ethanol for ~ 15 min.Then a certain amount of the FeP suspension was drop-casted onto the surface of $BiVO_4$ electrodes (1 cm × 1 cm), and dried at room temperature. Meanwhile, for comparison, Fe_2P nanoparticles suspension was used as a cocatalyst replacing FeP to prepare $Fe_2P/BiVO_4$ photoanode composite under the same conditions.

2.3 Characterization

Power X-ray diffraction (XRD) patterns were obtained from X-ray diffraction (XRD, D/max–TTR III) using graphite monochromatized Cu Kα radiation of 1.54178 Å at a scanning rate of 5/min. The accelerating voltage and applied current were 40 kV and 200 mA, respectively. The scanning electron microscopy (SEM) images and energy-dispersed X-ray (EDX) analysis were performed using a JSM-6700F field emission scanning electron microscopy (FE–SEM). Transmission electron microscopy (TEM) images and high resolution transmission electron microscopy (HRTEM) images were obtained from a JEM-2010 electron microscopy, operated at an acceleration voltage of 200 kV. The UV–vis absorption spectra of the samples were carried out on a SOLID 3700 UV–vis spectrometer. X-ray photoelectron spectroscopy (XPS) were acquired with a Thermo ESCALAB 250 X-ray photoelectron spectroscopy instrument.

2.4 Photoelectrochemical Measurements

Photoelectrochemical performances of photoanodes were measured in a typical three-electrode configuration with an Ag/AgCl (~ 4 M KCl solution) reference electrode and a platinum foil counter electrode. The simulated solar illumination was obtained from a 300 W Xenon arc lamp equipped with an AM 1.5G filter, and the power intensity of the incident light reached at the surface of the working electrodes was carefully calibrated to 100 mW/cm^2. 1 M potassium borate buffer solution was used as the electrolyte for photoelectrochemical measurements. For sulfite oxidation, an additional 0.2 M Na_2SO_3 solution was added into the electrolyte as a hole scavenger. Back-side illumination with exposed area of 1 cm^2 (1 cm × 1 cm) was carried out in a glass cell with ~ 40 mL of electrolyte. Photocurrent-potential curves were obtained on an electrochemical workstation (Model CHI660E, purchased from Shanghai Chen Hua Instrument Co., Ltd.) with a scan rate of 10 mV/s. The recorded potential versus Ag/AgCl was converted against RHE according to the Nernst equation $E_{RHE} = E_{Ag/AgCl} + 0.059 \times pH + 0.197$.

Applied bias photon-to-current efficiency (ABPE) can be calculated using the following equation: $ABPE = ((1.23 - V_{RHE}) \times \frac{J_{light} - J_{dark}}{P_{light}}) \times 100\%$, where V_{RHE} represents the applied potential vs RHE, J_{light} and J_{dark} are the measured photocurrent and dark current density (mA/cm^2), respectively. P_{light} (100 mW/cm^2) is the power density of AM 1.5 G.

Electrochemical impedance spectra (EIS) were measured in 1 M potassium borate (pH = 9) by applying a voltage amplitude of 5 mV with the frequency range from 100 kHz to 0.01 Hz under the open-circuit potential and AM 1.5G illumination. The Mott–Schottky plots were obtained in 1 M potassium borate (pH = 9) at a preset frequency of 1000 Hz using an AC amplitude of 10 mV in the dark.

3 Results and Discussion

3.1 XRD Analysis

Pristine $BiVO_4$ electrodes were synthesized by electrodeposition and annealing in air described in previous literature. The FeP nanoparticles were prepared from Fe_3O_4 via a phosphorization process and loaded onto the nanoporous $BiVO_4$ electrodes by a drop-casting method.The crystalline phases composition of pristine $BiVO_4$, pristine FeP nanoparticle along with the $FeP/BiVO_4$ composites were analyzed by X-ray diffraction. Figure 1a shows the XRD patterns of Fe_3O_4 sample and the corresponding FeP. After phosphorization, the diffraction peaks located at 22.9°, 30.8°, 32.7°, 34.5°, 37.2°, 45.5°, 46.3°, 47.1°, 48.3° and 50.4° were observed, which were indexed to the (101), (002), (112), (011), (200), (112), (200) (202), (211) and (103) planes of orthorhombic FeP (PDF#78–1443), respectively. Meanwhile, the crystal texture of the as-prepared BiOI and $BiVO_4$ photoanodes were further confirmed by XRD patterns (Fig. 1b). As shown in Fig. 1b, all the peaks can be indexed to tetragonal BiOI (PDF#10–0445) and monoclinic $BiVO_4$ (PDF#14–0688), respectively [27]. However, no peak attributed to FeP was observed from the XRD pattern of $FeP/BiVO_4$ composites, which may be due to its low loading amount of FeP sample.

3.2 Microstructures and Compositions Analysis

The microstructures of the photoelectrodes composites were investigated using SEM and TEM characterization. Figure 2a displays the BiOI nanoplates with a thickness of ~20 nm were possessed with sufficient voids.Meanwhile,

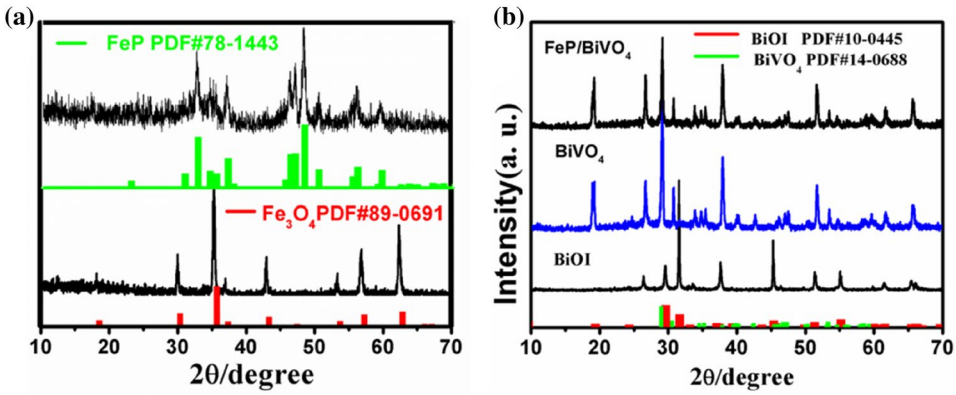

Fig. 1 XRD patterns of Fe_3O_4, FeP, BiOI, $BiVO_4$ together with FeP/$BiVO_4$

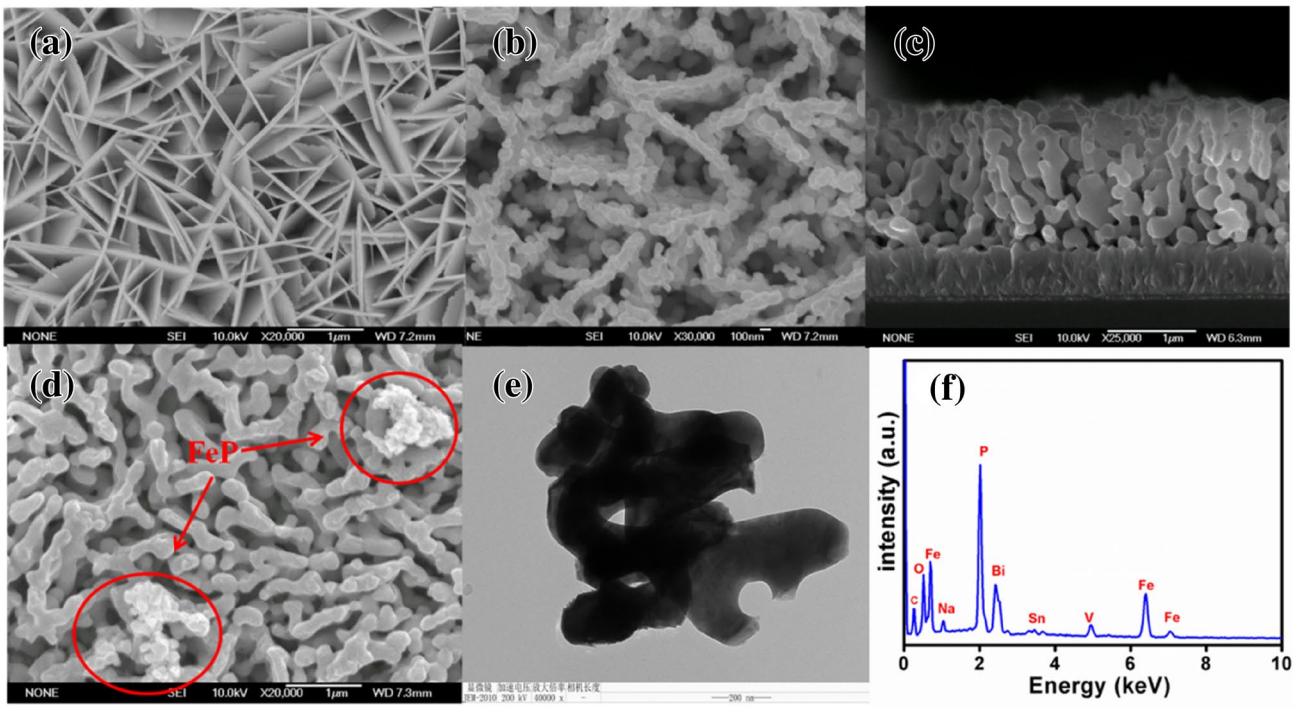

Fig. 2 Compositions and morphologies of BiOI, $BiVO_4$ together with FeP/$BiVO_4$ composites

as shown in Fig. 2b, c, the nanoporous network of $BiVO_4$ photoelectrodes were confirmed by the top-view and side-view SEM analysis respectively. Compared with pure $BiVO_4$, Fig. 2d unambiguously reveal FeP nanoparticles, marked as the red circle, were successfully deposited on $BiVO_4$ surface.In order to furtherly confirm the existence of FeP nanoparticles, as seen in Fig. 2f, the EDX analysis of FeP/$BiVO_4$ reveals the presence of Co, P, Bi, V and O elements, implying the FeP nanoparticles were successfully loaded onto the $BiVO_4$ photoelectrode. Meanwhile, TEM analysis was used to investigate the FeP/$BiVO_4$ composite. As shown in Fig. 2e, it is also found that FeP nanoparticles were deposited on $BiVO_4$ surface.

3.3 XPS Analysis

With aim to further investigate the valence state and chemical composition of FeP/$BiVO_4$ photoanode, the XPS spectra of FeP/$BiVO_4$ were examined. The XPS survey spectrum of FeP/$BiVO_4$ showed the sample surface presence of Fe, P, Bi, C, V and O elements (Fig. 3a), as well as the O element is attributed to surface partly oxidation of FeP, and the C element derived from the reference. Furthermore, the high resolution XPS spectrum of Bi $_{4f}$ (~ 159.4 eV and ~ 164.5 eV) and V_{2p} (~ 516.8 eV and ~ 524.5 eV) were well matched to the reported values of monoclinic $BiVO_4$ (Fig. 3b, c).As shown in Fig. 3d, the two peaks at ~ 130.5 eV and ~ 129.6 eV,

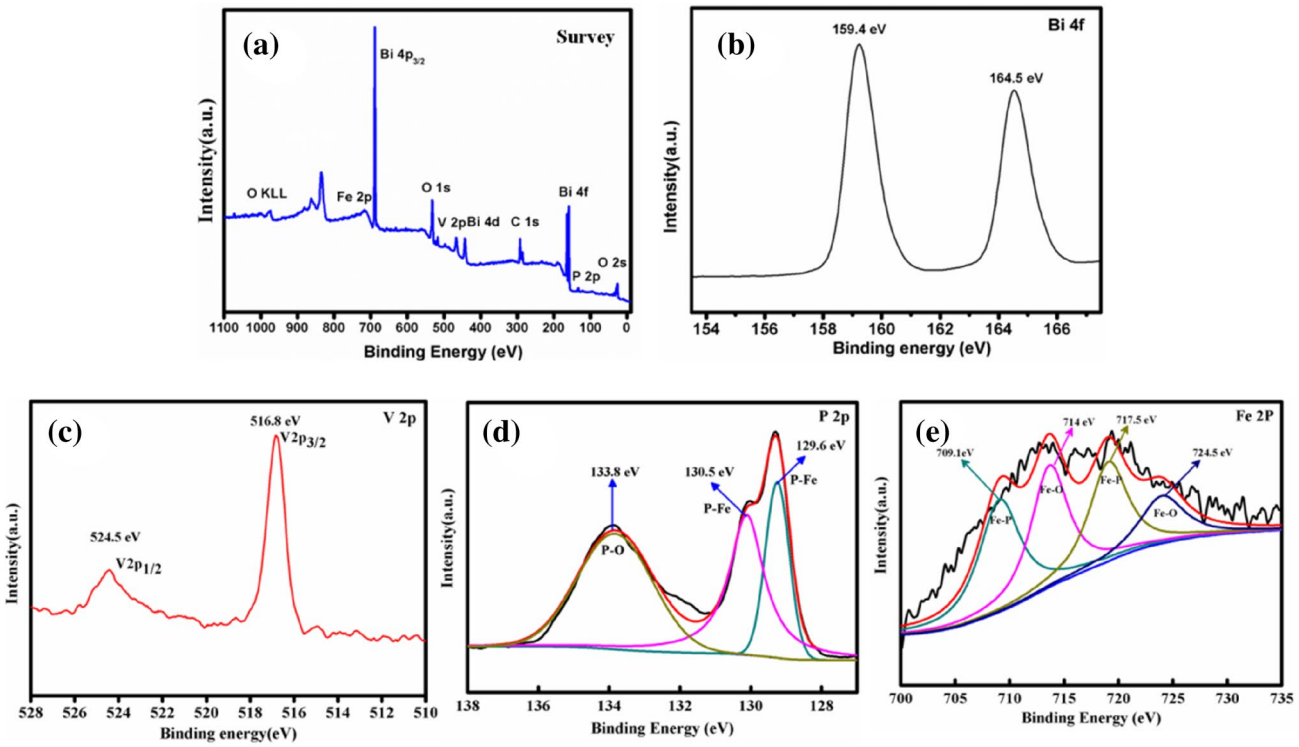

Fig. 3 **a** XPS survey spectra and high-resolution XPS spectra of. **b** Bi 4f. **c** V2p. **d**P 2p, and **f** Fe 2p of the FeP/$BiVO_4$ sample

which can be assigned to the low binding energy of P 2p1/2 and P 2p3/2 in FeP, respectively [31]. Meanwhile, the spectrum of P 2p also exhibits a peak with high binding energy of ~ 133.8 eV, which may be due to partial oxidation of P element, such as phosphate. Furthermore, as shown in Fig. 3e, the two peaks at ~ 709.1 eV and ~ 717.5 eV likely corresponding to the Fe $2p_{3/2}$ and Fe $2p_{1/2}$ peaks in FeP, respectively [42]. The other two peaks at binding energies of ~ 714 eV and ~ 724.5 eV, which arises from the iron oxide [43]. Hence, these above results further reveal that FeP cocatalyst nanoparticles were successfully deposited on surface of the worm-like nanoporous $BiVO_4$.

3.4 UV–Vis Analysis

In order to gain the light harvesting properties of pristine $BiVO_4$ and FeP/$BiVO_4$ hybrid, the UV–vis diffuse reflectance spectroscopy technique were investigated. As demonstrated in Fig. 4a, the UV–vis absorption spectra of $BiVO_4$ and FeP/$BiVO_4$ exhibited the identical absorption edge at around 525 nm, which are consistent with the optical band gap energy of ~ 2.47 eV (Fig. 4b), manifesting that FeP cocatalyst nanoparticles were not doped into the monoclinic $BiVO_4$ crystal lattice to without change its band gap.

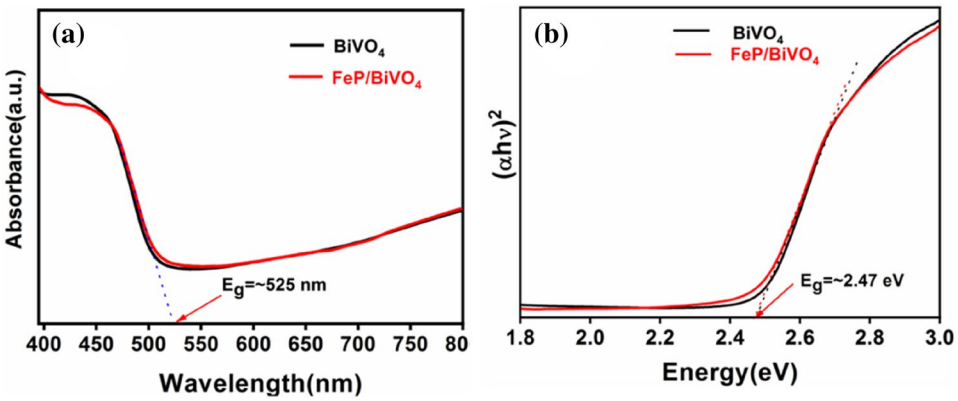

Fig. 4 **a** The optical absorption spectroscopy of the bare $BiVO_4$ and FeP/$BiVO_4$; **b** Tauc plot of bare $BiVO_4$ and FeP/$BiVO_4$

3.5 Photoelectrochemical Water Oxidation

All the PEC performances of photoanodes in this study were acquired according to back-side illumination, which was due to the poor electron transport property and long electron transfer distance of the relative thick photoanode under front-side illumination. As exhibited in Fig. 5b. The pristine $BiVO_4$ exhibited a photocurrent density of ~ 1.88 mA/cm^2 at 1.23 V vs. RHE and the cathodic shift (~430 mV) in the onset potential. The maximum photocurrent density of FeP/$BiVO_4$ photoanode hybrid for PEC solar water oxidation could reached ~ 3.05 mA/cm^2 under optimal amount of FeP nanoparticles(Fig. 5b), which is ~ 1.6 times higher than that of the unmodified pritine $BiVO_4$.

So as to identify the surface reaction kinetics of $BiVO_4$-based photoanodes, 0.2 M Na_2SO_3 solution was served as a hole scavenger. As shown in Fig. 5c, an obvious distinction of $BiVO_4$ between Na_2SO_3 solution and water oxidation under dark condition. The poor water oxidation kinetic of $BiVO_4$ photoanode, resulting in the serious surface charge recombination. However, after the loading of FeP nanoparticles, a dramatic cathodic shift of onset potential for water oxidation compared to the curve of bare $BiVO_4$ was observed, indicating the FeP is an active dark electrocatalyst for oxygen evolution. Meanwhile, Fig. 5d displays an identical PEC sulfite oxidation property of $BiVO_4$ and FeP/$BiVO_4$, indicating the similar charge separation efficiency in the bulk upon loading of FeP nanoparticles. Thus, the significant suppression of the surface recombination by loading of FeP nanoparticles could improve PEC property of solar-driven water oxidation. For comparation, the Fe_2P nanoparticles were used as cocatalyst, which exhibits a lower photocurrent density than that of FeP nanoparticles, highlighting FeP nanoparticles is an active cocatalyst for solar water splitting (Fig. 5e).

As demonstrated in Fig. 5f, before FeP modification, the $\eta_{surface}$ of $BiVO_4$ photoanode is ~ 40% at 1.23 V vs. RHE, indicating more than half of the photogenerated holes are captured by charge recombination at the surface of pristine $BiVO_4$ photoanode. Interesting phenomenon is the $\eta_{surface}$ of FeP/$BiVO_4$ could reached ~ 57% at 1.23 V vs RHE, which was much higher than that of the pure $BiVO_4$ photoanode. Base on above analysis, FeP nanoparticles could efficiently decrease the surface recombination losses at the surface of $BiVO_4$ photoanodes.

3.6 Photoelectrochemical Mechanism

To further investigated the interface charge transport behavior of the photoanodes charge carries, the photocurrent transients of $BiVO_4$ and FeP/$BiVO_4$ photoanodes were recorded in Fig. 6a. During each light on–off cycle process, incisive photocurrent transient spike was observed for bare $BiVO_4$ photoanode, indicating partly surface charge recombination. Meanwhile, the maximum photocurrent density of FeP/$BiVO_4$ for PEC water oxidation could reached ~ 2.85 mA/cm^2 at 1.23 V vs RHE. The Mott–Schottky (MS) curves of the photoelectrodes were shown in Fig. 6b. Compared

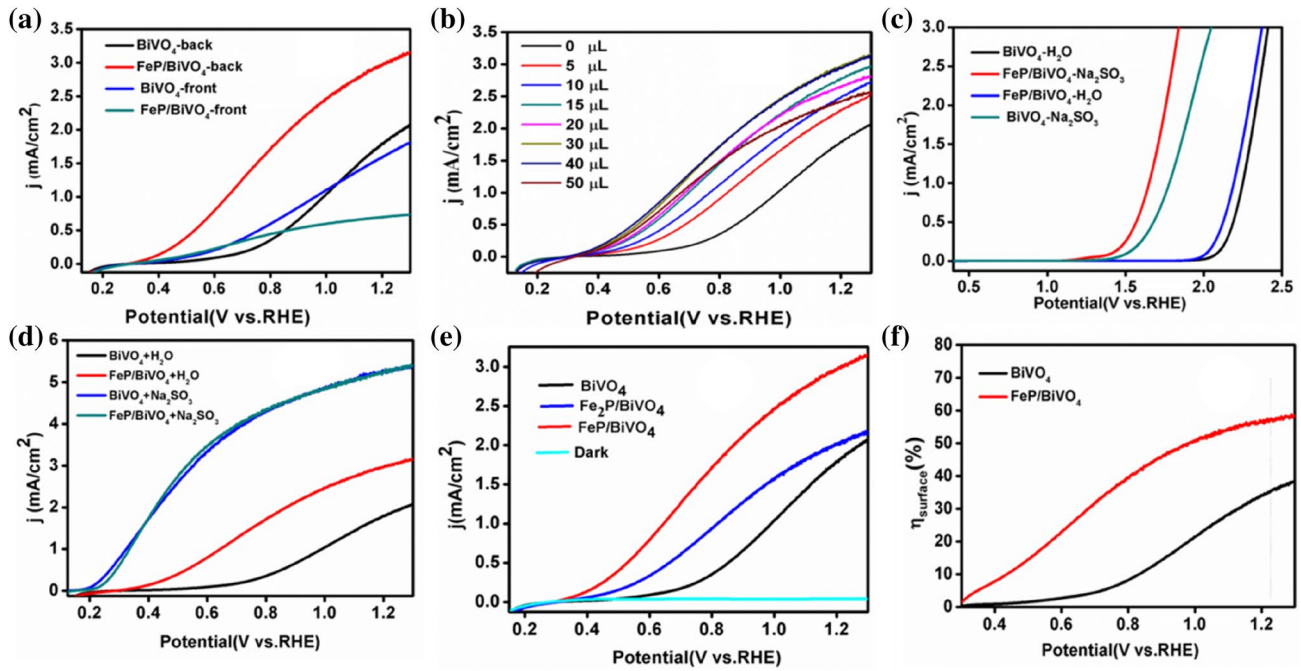

Fig. 5 Photoelectrochemical performances of photoanodes under differen conditions

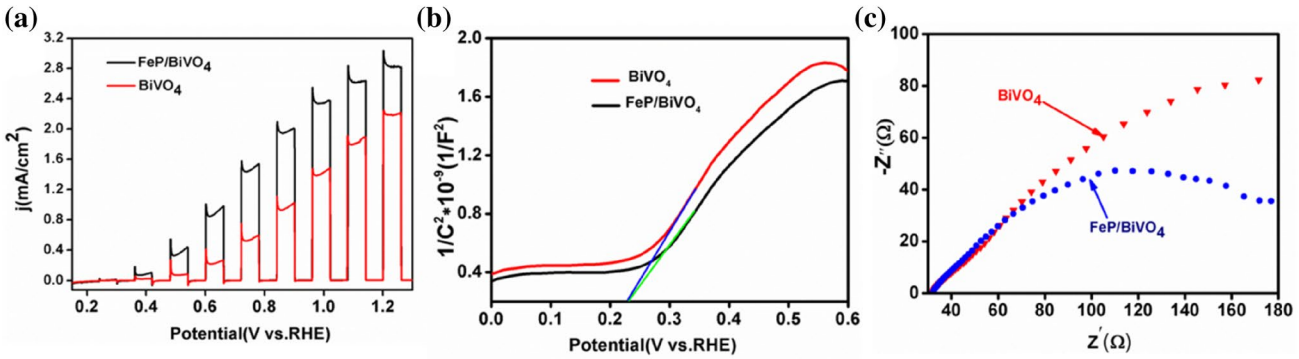

Fig. 6 **a** The photocurrent transients of $BiVO_4$ and FeP/$BiVO_4$. **b** Mott–Schottky curves of $BiVO_4$ and FeP/$BiVO_4$ **c** EIS curves for $BiVO_4$ and FeP/$BiVO_4$

with bare $BiVO_4$, the FeP/$BiVO_4$ composites exhibited the identical flat band potential. Thus, the dramatically enhanced PEC properties of FeP/$BiVO_4$ hybrid may be attributed to improve surface charge transfer efficiency. Furthermore, the electrochemical impedance spectroscopy (EIS) of $BiVO_4$ and FeP/$BiVO_4$ were performed. As shown in Fig. 6c, compared with naked $BiVO_4$ photoanode, a much smaller semidiameter of the semicircle was observed for FeP/$BiVO_4$ under open-circle potential and AM 1.5G illumination, indicating a relatively favorable interfacial charge transfer ability of FeP/$BiVO_4$. in accordance with the quantification analysis results of the surface charge separation efficiency.

The maximum applied bias photon-to-current efficiency (ABPE) for FeP/$BiVO_4$ was calculated to be ~ 0.53% at 0.6 V vs RHE (Fig. 7a), which was much higher than that of the unmodified $BiVO_4$. Moreover, the PEC stability of the FeP/$BiVO_4$ photoanode was conducted in 1 M potassium borate solution at 0.6 V vs RHE. As shown in Fig. 7b, the photocurrent density gradually decreased during the consecutive light illumination in ~ 30 min, probably on account of the slowly drop of FeP nanoparticles into solution or the intrinsic instability of the FeP/$BiVO_4$ photoanode.However, the photocurrent density gradually increased after ~ 30 min light illumination, which was probably resulted from the other active substance (For example FeOOH).

4 Conclusion

In summary, decoration of $BiVO_4$ photoanode surface with a novel FeP nanoparticles has achieved a improving photocurrent density for PEC water splitting for the first time, which is ~ 1.6 times higher than that of the bare $BiVO_4$ photoanode. The highly efficient suppression of surface recombination through FeP modification was also certified by PEC measurements using 0.2 M Na_2SO_3 solution as a hole scavenger. Meanwhile, the maximum ABPE of FeP/$BiVO_4$ photoanodes was ~ 0.53% at 0.6 V vs RHE. Furthermore, the FeP/$BiVO_4$ photoanode was prepared by inexpensive noble-metal-free materials, will provide insights on the design and development of efficient water splitting $BiVO_4$-based photoanodes.

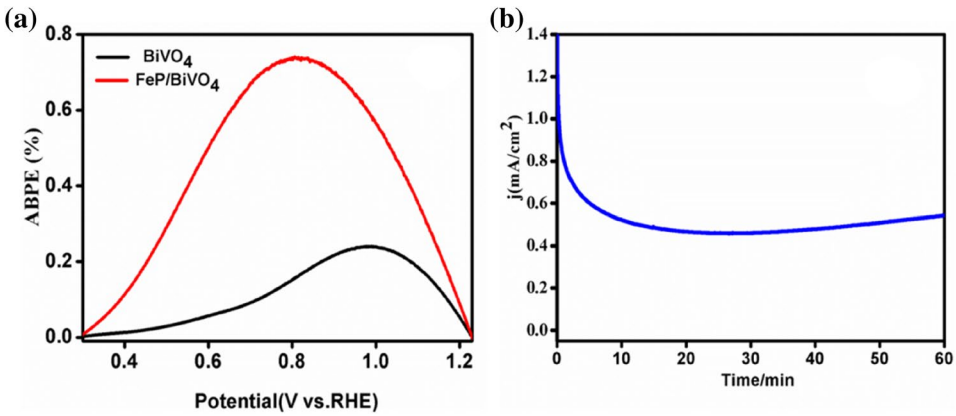

Fig. 7 **a** ABPE curves for $BiVO_4$ and FeP/$BiVO_4$. **b** Stability test carried out for FeP/$BiVO_4$ at a constant potential of 1.23 V vs RHE

Acknowledgements The funds support were mainly received from the National Key Research and Development Program of China (Grant No. 2017YFA0402800), National Natural Science Foundation of China (Grant No. 51772285, 21473170, and 51878004), and the Natural Science Fund of Anhui Province (Grant No. 1808085ME139).

Compliance with Ethical Standards

Conflict of interest All the authors in this work declare no competing financial interest.

References

1. Fujishima A, Honda K (1972) Nature 238:37–38
2. Rausch B, Symes MD, Chisholm G et al (2014) Science 345(6202):1326–1330
3. Jaramillo TF, Jørgensen KP, Bonde J et al (2007) Science 317(5834):100
4. Ge J, Liu Y, Jiang D et al (2019) Chin J Catal 40(2):160–167
5. Ge J, Jiang D, Zhang L et al (2018) Catal Lett 148(12):3741–3749
6. Zhang L, Jiang D, Irfan RM et al (2019) Journal of Energy. Chemistry 30:71–77
7. Ho-Kimura S, Moniz SJA, Handoko AD et al (2014) J Mater Chem A 2(11):3948–3953
8. Chou J-C, Yang M-H, Liao J-W et al (2014) Mater Chem Phys 143(3):1417–1422
9. Xu K, Chatzitakis A, Norby T (2017) Photochem Photobiol Sci 16(1):10–16
10. Wang W, Dong J, Ye X et al (2016) Small 12(11):1469–1478
11. Zhang Z, Chen B, Baek M et al (2018) ACS Appl Mater Interfaces 10(7):6218–6227
12. Wang R, Qiu G, Xiao Y et al (2019) J Catal 374:378–390
13. Lee T, Lee Y, Jang W et al (2016) J Mater Chem A 4(29):11498–11506
14. Zhang J, Zhang P, Wang T et al (2015) Nano Energy 11:189–195
15. Jiang D, Yue Q, Tang S et al (2018) J Catal 366:275–281
16. Dias P, Vilanova A, Lopes T et al (2016) Nano Energy 23:70–79
17. Cho IS, Han HS, Logar M et al (2016) Adv Energy Mater 6(4):1501840
18. Wang D, Zhang Y, Wang J et al (2014) ACS Appl Mater Interfaces 6(1):36–40
19. Li M, Luo W, Yang L et al (2016) Aust J Chem 69(6):631–637
20. Zhang P, Wang T, Zhang J et al (2015) Nanoscale 7(31):13153–13158
21. Wang Y-C, Chang C-Y, Yeh T-F et al (2014) J Mater Chem A 2(48):20570–20577
22. Yang L-H, Luo W-J, Li M-X et al (2016) Chinese. J Inorg Chem 32(10):1839–1846
23. Li M, Luo W, Cao D et al (2013) Angew Chem Int Ed 52(42):11016–11020
24. Luo W, Yang Z, Li Z et al (2011) Energy Environ Sci 4(10):4046–4051
25. Tao X, Shao L, Wang R et al (2019) J Colloid Interface Sci 541:300–311
26. Monfort O, Pop L-C, Sfaelou S et al (2016) Chem Eng J 286:91–97
27. Kim TW, Choi K-S (2014) Science 343(6174):990–994
28. Ye K-H, Chai Z, Gu J et al (2015) Nano Energy 18:222–231
29. Jiao Z, Zheng J, Feng C et al (2016) Chemsuschem 9(19):2824–2831
30. Zhong DK, Choi S, Gamelin DR (2011) J Am Chem Soc 133(45):18370–18377
31. Ding C, Shi J, Wang D et al (2013) Phys Chem Chem Phys 15(13):4589–4595
32. Yang J, Wang D, Han H et al (2013) Acc Chem Res 46(8):1900–1909
33. Suen N-T, Hung S-F, Quan Q et al (2017) Chem Soc Rev 46(2):337–365
34. Yu F, Li F, Yao T et al (2017) Acs Catalysis 7(3):1868–1874
35. Seabold JA, Choi K-S (2012) J Am Chem Soc 134(4):2186–2192
36. Son CY, Kwak IH, Lim YR et al (2016) Chem Commun 52(13):2819–2822
37. Cheng H, Lv XJ, Cao S et al (2016) Sci Rep 6:19846
38. Jiang P, Liu Q, Liang Y et al (2014) Angew Chem Int Ed Engl 53(47):12855–12859
39. Sun Z, Chen H, Huang Q et al (2015) Catalysis. Sci Technol 5(11):4964–4967
40. Yuan Y, Pei H, Chen H et al (2017) Catal Commun 100:202–205
41. Chen X, Zhang Z, Li X et al (2006) Chem Phys Lett 422(1–3):294–298
42. Yu Y, Peng Z, Asif M et al (2018) Acs Sustain Chem Eng 6(9):11587–11594
43. Guo X, Feng Z, Lv Z et al (2017) Chemelectrochem 4(8):2052–2058

Affiliations

Jianhua Ge[1,2] · Xiulong Ding[1] · Daochuan Jiang[2] · Lei Zhang[2] · Pingwu Du[2]

[1] School of Earth and Environment, Anhui University of Science & Technology, Huainan, Anhui Province 232001, People's Republic of China

[2] CAS Key Laboratory of Materials for Energy Conversion, Department of Materials Science and Engineering, Collaborative Innovation Center of Chemistry for Energy Materials(iChEM), University of Science and Technology of China (USTC), Hefei, Anhui Province 230026, People's Republic of China